Mapping the Galactic centre's dark cluster via resonant relaxation

Kerwann Tep, Jean-Baptiste Fouvry, Christophe Pichon, Gernot Heissel, Thibaut Paumard, Guy Perrin, Frederic Vincent

Monthly Notices
of the
ROYAL ASTRONOMICAL SOCIETY

MNRAS **506,** 4289–4301 (2021)
Advance Access publication 2021 July 12

https://doi.org/10.1093/mnras/stab1945

Mapping the Galactic centre's dark cluster via resonant relaxation

Kerwann Tep,[1]★ Jean-Baptiste Fouvry,[1] Christophe Pichon,[1,2,3] Gernot Heißel,[4] Thibaut Paumard,[4] Guy Perrin[4] and Frederic Vincent[4]

[1]*CNRS and Sorbonne Université, UMR 7095, Institut d'Astrophysique de Paris, 98 bis Boulevard Arago, F-75014 Paris, France*
[2]*Korea Institute for Advanced Study, 85 Hoegiro, Dongdaemun-gu, 02455 Seoul, Republic of Korea*
[3]*IPhT, DRF-INP, UMR 3680, CEA, Orme des Merisiers Bat 774, F-91191 Gif-sur-Yvette, France*
[4]*LESIA, Observatoire de Meudon, 5 Place Jules Janssen, F-92190 Meudon, France*

Accepted 2021 July 2. Received 2021 June 22; in original form 2021 March 19

ABSTRACT

Supermassive black holes in the centre of galaxies dominate the gravitational potential of their surrounding stellar clusters. In these dense environments, stars follow nearly Keplerian orbits, which get slowly distorted as a result of the potential fluctuations generated by the stellar cluster itself. In particular, stars undergo a rapid relaxation of their eccentricities through both resonant and non-resonant processes. An efficient implementation of the resonant diffusion coefficients allows for detailed and systematic explorations of the parameter space describing the properties of the stellar cluster. In conjunction with recent observations of the S-cluster orbiting SgrA*, this framework can be used to jointly constrain the distribution of the unresolved, old, background stellar cluster and the characteristics of a putative dark cluster. Specifically, we show how this can be used to estimate the typical mass and cuspide exponent of intermediate-mass black holes consistent with the relaxed state of the distribution of eccentricities in the observed S-cluster. This should prove useful in constraining supermassive black hole formation scenarios.

Key words: diffusion – gravitation – galaxies: kinematics and dynamics – galaxies: nuclei.

1 INTRODUCTION

Galactic nuclei are among the densest stellar systems of the universe. Recent outstanding observations keep providing us with new information on these regions. These include detailed census of stellar populations around SgrA* in the centre of the Galaxy (Ghez et al. 2008; Gillessen et al. 2017), the first observation of the relativistic precession of the star S2 within our own Galactic centre (Gravity Collaboration 2020); the observation of a cool accretion disc around SgrA* (Murchikova et al. 2019); the first image of the shadow of M87 (Event Horizon Telescope Collaboration 2019) and mergers of binary black holes recently detected via gravitational wave emission (Abbott et al. 2019), that may or may not have occurred in galactic nuclei. These various successes will soon be complemented with ever finer resolution around SgrA* (Gravity Collaboration 2017), as well as much larger stellar populations permitted by the planned upgrade on VLTI/GRAVITY (Eisenhauer 2019; Gravity Collaboration 2021), as well as the upcoming thirty-metre class telescopes such as TMT (Do et al. 2019) and ELT/MICADO (Davies et al. 2018; Pott et al. 2018). Such a wealth of observational information offers new venues to investigate the details of stellar dynamics around supermassive black holes (BHs), as well as probe the possible presence of intermediary mass black holes (IMBHs) in these regions (Portegies Zwart & McMillan 2002).

Indeed, in the crowded region of galactic nuclei, the gravitational potential remains none the less dominated by the central supermassive BH. Because of the steep gravitational potential that this BH induces, galactic nuclei involve a wide range of relaxation processes and time-scales (Rauch & Tremaine 1996; Hopman & Alexander 2006; Merritt 2013; Alexander 2017). These are: (i) the dynamical time associated with the fast Keplerian motion imposed by the central BH (∼16 yr for S2, e.g. Gillessen et al. 2017). On longer time-scales, one can formally smear out the stars along their stellar orbits so that they are effectively replaced with massive eccentric wires; (ii) the in-plane precession time of the Keplerian wires generated by both the relativistic corrections from the central BH and the stellar mean potential (∼3×10^4 yr for S2, e.g. Gravity Collaboration 2020); (iii) the vector resonant relaxation (VRR) time (see e.g. Kocsis & Tremaine 2015; Fouvry, Bar-Or & Chavanis 2019) during which, as a result of the non-spherically symmetric stellar fluctuations and relativistic corrections induced by a spinning BH, stars undergo a stochastic reshuffling of their orbital orientations (∼1 Myr for S2, e.g. Kocsis & Tremaine 2011); (iv) the scalar resonant relaxation (SRR) time (Rauch & Tremaine 1996; Bar-Or & Alexander 2016; Sridhar & Touma 2016; Bar-Or & Fouvry 2018) during which resonant torques between the in-plane precessing wires lead to a diffusion of the wires' eccentricities (∼10 Myr for S2, e.g. Bar-Or & Fouvry 2018); (v) the non-resonant relaxation (NR) time (Bahcall & Wolf 1976; Lightman & Shapiro 1977; Bar-Or, Kupi & Alexander 2013; Vasiliev 2017) during which nearby pairwise scatterings slowly drive the long-term relaxation of the wires' semimajor axes, as well as of their eccentricities (∼1 Gyr for S2, e.g. Kocsis & Tremaine 2011).

The leverage provided by modelling these dynamical processes with recent observations should allow us to constrain hidden features of the Galactic centre. Here, we will focus on the relaxation of stellar eccentricities in galactic nuclei, through processes (iv) and (v).

★ E-mail: tep@iap.fr

Indeed, as emphasized in Gillessen et al. (2017) (see fig. 13 therein), the S-cluster orbiting SgrA* (for $a \simeq 5$ mpc) has been observed with a significantly relaxed distribution of eccentricities. Detailed spectroscopic observations (Habibi et al. 2017) also provide us with well constrained main-sequence ages for these same stars. The age of the young B-stars at a distance of $\sim$10 mpc from the BH is comparable to the resonant relaxation time, implying that resonant relaxation may have played an important role in their dynamical structure (Hopman & Alexander 2006). Hence, any credible diffusion mechanism has to be efficient enough to drive a significant eccentricity relaxation of the S-stars within their lifetime. Equivalently, one may use this constraint as a dynamical probe to further characterize the properties of the unresolved old stellar and putative dark cluster, which both drive the relaxation of the S-stars themselves (see e.g. Generozov & Madigan 2020). Following Merritt, Gualandris & Mikkola (2009), Antonini & Merritt (2012), Monte Carlo simulations have similarly shown that stellar mass BHs can reduce the resonant relaxation time near the present-day location of the S-stars to $\sim$10 Myr, which is of the order of the age of the S-stars (Habibi et al. 2017). This is the purpose of this paper. We use kinetic theory to constrain the range of cluster models for SgrA* that are compatible with the observational requirement of having significantly relaxed S-stars eccentricities.

The paper is organized as follows. In section 2, we briefly review the two main dynamical processes in galactic nuclei through which stars can relax in eccentricities. We also detail our (fast) numerical computations of the associated diffusion coefficients. In section 3, we place first constraints on the stellar distribution of the unresolved old (stellar and dark) cluster using these diffusion process in conjunction with recent observations of the S-cluster. We also present a fiducial model in which we can vary the number of stars to anticipate what upcoming instruments will be able to measure. Finally, we discuss these results and conclude in section 4.

2 LONG-TERM RELAXATION

2.1 Mean-field dynamics

Let us consider a test star orbiting within a galactic nuclei containing a central supermassive BH of mass $M_\bullet$. Because the potential is dominated by the central BH, this test star follows a (nearly) Keplerian orbit that we can describe using orbital elements (Murray & Dermott 1999) written as $(M, \omega, \Omega, J_c, J, J_z)$. In these notations, the dynamical angles are M the mean anomaly, i.e. the location of the star along its Keplerian orbit, ω the argument of the pericentre, and Ω the longitude of the ascending node. The associated actions are given by

$$J_c = \sqrt{GM_\bullet a}; \quad J = J_c\sqrt{1-e^2}; \quad J_z = J\cos(I). \tag{1}$$

In that expression, J_c is the circular angular momentum, a the orbit's semimajor axis and e its eccentricity, J the magnitude of the angular momentum vector, I its inclination, and J_z its projection along the z-axis.

The fast Keplerian motion of the star is then described by $\dot{M} = \nu_{\rm Kep}$, with the Keplerian frequency

$$\nu_{\rm Kep}(a) = \sqrt{\frac{GM_\bullet}{a^3}}. \tag{2}$$

This dynamical time being so short, the traditional approach of secular dynamics is to smear out the stars along their Keplerian ellipses (see e.g. Touma, Tremaine & Kazandjian 2009), so that they formally become massive wires. Following this orbit-average over M, the conjugate coordinate J_c (and therefore a) is conserved by adiabatic invariance for the secular dynamics.

Describing the long-term dynamics of stellar orbits in galactic nuclei amounts then to describing the long-term evolution of the remaining five coordinates $\{\omega, \Omega, J_c, J, J_z\}$. On longer time-scales, the wires undergo some in-plane precession, described by

$$\frac{{\rm d}\omega}{{\rm d}t} = \nu_{\rm p}(a, j) = \nu_{\rm GR}(a, j) + \nu_{\rm M}(a, j). \tag{3}$$

Here, $\nu_{\rm p}(a, j)$ describes the total precession frequency of the wire's pericentre. It is given by the joint contribution from the relativistic corrections from the central BH, i.e. the Schwarzschild precession (Merritt 2013), through the term $\nu_{\rm GR}(a, j)$, as well as from the mass precession imposed by the mean background stellar cluster, $\nu_{\rm M}(a, j)$. Appendix A presents explicit expressions of both of these frequencies.

As mentioned in introduction, on time-scales longer than the precession time the Keplerian wires will be subject to three main relaxation processes, namely the VRR, during which the direction of the stellar orbital plane, $\widehat{\mathbf{J}} = (\Omega, I)$, diffuses; the SRR, during which J, i.e. the eccentricity e, diffuses; and finally, the NR, during which both (J_c, J) diffuse, i.e. wires undergo changes in both a and e. Here, we are interested in the process of eccentricity relaxation. Stellar eccentricities can relax both through SRR and NR, and we now briefly recall the key properties of these two processes.

2.2 Eccentricity relaxation

We are interested in the dynamics of the S-stars on time-scales of the order of $\sim$10 Myr, i.e. their stellar age. Since this age is generically much shorter than the time-scale for NR, we may assume that the semimajor axis of each star, a, is conserved. As a consequence, we keep track of the stars' eccentricities through the dimensionless angular momentum

$$j = \sqrt{1-e^2}. \tag{4}$$

Characterizing the relaxation of the S-stars amounts then to describing the long-term dynamics of their j.

This diffusion is sourced by the potential fluctuations generated by the background unresolved cluster. This cluster is expected to be old, i.e. has been orbiting around SgrA* for a time much longer than the SRR relaxation time. As such, we may assume that it has already fully relaxed all its orbital elements. We therefore assume that it has a spherically symmetric distribution of orientations, and, importantly, follows a thermal distribution of eccentricities.

In that limit, the eccentricities of the test particles, i.e. the eccentricities of the S-stars, follow a diffusion equation of the form (Bar-Or & Alexander 2016)

$$\frac{\partial P(j,t\,|\,a)}{\partial t} = \frac{1}{2}\frac{\partial}{\partial j}\left[j\,D_{jj}(a,j)\,\frac{\partial}{\partial j}\left(\frac{P(j,t\,|\,a)}{j}\right)\right], \tag{5}$$

where $P(j, t\,|\,a)$ describes the probability distribution function (PDF) of test stars' eccentricities, j, for a given semimajor axis a, as a function of time, normalized so that $\int {\rm d}j\, P(j, t\,|\,a) = 1$. The flux is conserved because the boundary conditions are such that there is, by design, no flux that escapes the [0, 1] interval. Indeed, at $j = 0$, the flux vanishes because of the j-factor in equation (5), while at $j = 1$, the diffusion coefficient D_{jj} goes to 0. We neglect the supermassive BH's loss-cone region, which would drive a small exiting flux at low j. Finally, we also neglect the diffusion in a (hence $D_{aa} = 0$), which is minor compared to that in angular momentum j (Bar-Or & Alexander 2016). Stars diffuse therefore at fixed semimajor axes.

The steady state of equation (5) is given by the thermal solution, $P_{\rm th}(j\,|\,a) = 2j$, i.e. the eccentricity PDF also followed by the background stars. Let us already note that equation (5) can be rewritten under the more classical Fokker–Planck (FP) form as

$$\frac{\partial P(j,t|a)}{\partial t} = -\frac{\partial}{\partial j}[D_j(a,\,j)\,P(j,\,t|a)] + \frac{1}{2}\frac{\partial^2}{\partial j^2}[D_{jj}(a,\,j)\,P(j,\,t|a)], \tag{6}$$

where the first- and second-order diffusion coefficients satisfy the fluctuation-dissipation relation (Bar-Or & Alexander 2016)

$$D_j = \frac{1}{2j}\frac{\partial}{\partial j}[j\,D_{jj}]. \tag{7}$$

The rewriting from equation (6) is useful to perform Monte Carlo integrations of the stochastic dynamics, as presented in Appendix D.

In equation (5), we introduced the diffusion coefficient in angular momentum, $D_{jj}(a,\,j)$, that are the sum of two contributions

$$D_{jj}(a,\,j) = D^{\rm RR}_{jj}(a,\,j) + D^{\rm NR}_{jj}(a,\,j), \tag{8}$$

where $D^{\rm RR}_{jj}(a,\,j)$ captures the contribution from resonant relaxation (RR), while $D^{\rm NR}_{jj}(a,\,j)$ is associated with the contribution from NR. We now detail the content of each of these coefficients.

2.3 Scalar resonant relaxation

A first source of eccentricity relaxation stems from the long-range resonant couplings between the in-plane precessing wires. Following Bar-Or & Fouvry (2018) and references therein, the SRR diffusion coefficients read

$$D^{\rm RR}_{jj}(a,\,j) = \frac{4\pi G^2}{J_{\rm c}^2}\sum_{n=1}^{+\infty}\sum_{\substack{n'=-\infty\\ n'\neq 0}}^{+\infty}\frac{n^2}{|n'|} \times \int {\rm d}a'\,F_{\rm tot}(a',\,j')\frac{|A_{nn'}(a,\,j,\,a',\,j')|^2}{|\partial_j \nu_{\rm p}(a',\,j')|}, \tag{9}$$

where $J_{\rm c} = J_{\rm c}(a)$ was defined in equation (1), and j' is the implicit solution of the resonance constraint

$$\nu_{\rm p}(a',\,j') = \frac{n}{n'}\,\nu_{\rm p}(a,\,j), \tag{10}$$

with the in-plane precession frequencies, $\nu_{\rm p}(a,j)$, already introduced in equation (3).

In equation (9), we introduced the distribution function (DF), $F_{\rm tot}(a',\,j')$, to describe the background cluster, whose potential fluctuations are responsible for the long-term diffusion of stellar eccentricities. It is defined as

$$F_{\rm tot}(a,\,j) = \sum_i m_i^2 N_i(a)\,f_i(j|a), \tag{11}$$

where the sum over i runs over all the subpopulations of the background cluster. Each population is characterized by an individual mass, m_i, while $N_i(a)$ is the number of stars per unit semimajor axis a, and $f_i(j|a)$ is the conditional PDF of j for a given a, normalized so that $\int {\rm d}j f_i(j|a) = 1$. In practice, in order to ease the numerical resolution of the resonance condition (see Appendix A) and the computation of the NR diffusion coefficients, we assume that each population follows a power-law distribution in semimajor axes and is also fully relaxed in eccentricity, i.e. $f_i(j|a) = 2j$, owing to their old dynamical age. We further detail all our normalization conventions in Appendix B.

The resonant diffusion coefficients from equation (9) involve the coupling coefficients $|A_{nn'}|^2$ that describe the efficiency of the resonant coupling between two wires. They read

$$|A_{nn'}\left(a,\,j,\,a',\,j'\right)|^2 = 16\pi^2\sum_\ell \frac{|y^n_\ell|^2|y^{n'}_\ell|^2}{(2\ell+1)^3}\left|K^\ell_{nn'}\left(a,\,j,\,a',\,j'\right)\right|^2,$$

with the constant coefficients $y^n_\ell = Y^n_\ell(\frac{\pi}{2},\,\frac{\pi}{2})$, where the spherical harmonics are defined with the convention $\int {\rm d}\hat{\mathbf{r}}\,|Y^n_\ell(\hat{\mathbf{r}})|^2 = 1$. This equation involves the pairwise in-plane coupling coefficients $K^\ell_{nn'}$ that read

$$K^\ell_{nn'}(a,\,j,\,a',\,j') = \left\langle \cos(nf)\cos(n'f')\frac{{\rm Min}[r,\,r']^\ell}{{\rm Max}[r,\,r']^{\ell+1}}\right\rangle_{\circlearrowleft}, \tag{12}$$

where f is the true anomaly, while $\langle\,\cdot\,\rangle_{\circlearrowleft}$ stands for the orbit-average over both radial oscillations. Let us already emphasize that the coupling coefficients from equation (12) satisfy various symmetry properties. First, as imposed by $|y^n_\ell|^2$ and $|y^{n'}_\ell|^2$, these coefficients are non-zero only when $|n|,\,|n'| \leq \ell$, as well as $(\ell - n)$ and $(\ell - n')$ even. In addition, we note that we have $|A_{nn'}|^2 = |A_{\pm n\pm n'}|^2$, i.e. the strength of the $(n,\,n')$ coupling is independent of the sign of the resonance numbers. These are all important features which will allow us to reduce the required number of evaluations of the coupling coefficients. Finally, in practice, in equation (12), we truncate the harmonics up to a given $\ell_{\rm max}$.

In equation (12), the Min–Max terms stem from the usual Legendre expansion of the Newtonian interaction potential. The computation of $K^\ell_{nn'}$ is the overall bottleneck of the whole calculation of the SRR diffusion coefficients which we have to address. A naive inspection of equation (12) would lead us to believe that its computational complexity scales like $\mathcal{O}(K^2)$, with K the number of sampling points used to discrete both anomalies. Fortunately, one can take inspiration from multipole methods (see e.g. Fouvry et al. 2020) to compute them much more efficiently, yielding a computational complexity scaling like $\mathcal{O}(K)$. This is detailed in Appendix C.

Once the coupling coefficients have been estimated, we rely on equation (9) to evaluate the diffusion coefficients. This requires in particular to solve for the resonance condition from equation (10). For a given wire $(a,\,j)$ and a given resonance pair $(n,\,n')$, this amounts to finding all the wires $(a',\,j')$ for which the resonance condition $n\nu_{\rm p}(a,j) = n'\nu_{\rm p}(a',j')$ is satisfied. We detail in Appendix A our approach to solve the resonance condition, improving upon the method from Bar-Or & Fouvry (2018). The performance of the code is given in Table C1. The corresponding code is publicly available (see the data distribution policy below).

Fig. 1 gives an example of a computation of the RR diffusion coefficients for a fixed value of the semimajor axis. In particular, we recover the drastic damping of the RR diffusion coefficients for very eccentric orbits. This is due to the divergence of the relativistic precession frequencies for ever more eccentric wires, which prevents these wires from resonating with the bulk of the other wires (Merritt et al. 2011; Bar-Or & Alexander 2016). As can be noted from Fig. 1, very eccentric wires ($j \sim 0$) are then immune to the RR diffusion, and can only keep diffusing under the effect of the NR contributions.

2.4 Non-resonant relaxation

A second process through which test stars relax in eccentricities originates from NR (see §7.4.4 in Binney & Tremaine 2008). In that case, it is the slow build-up of nearby scatterings that ultimately drives the diffusion of their orbital parameters.

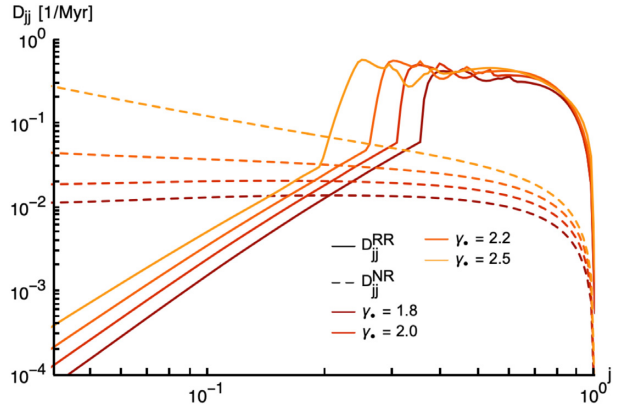

Figure 1. Illustration of the RR (full line) and NR (dashed line) diffusion coefficients. For the a Top-Heavy model (see section 3.1), we vary $\gamma_\bullet$ for a given value semimajor axis $a = 10$ mpc and the harmonic cutoff $\ell_{\max} = 10$. The diffusion coefficients go to 0 as $j \to 1$ (circular orbits), while the RR ones get drastically reduced for very eccentric orbits (Merritt et al. 2011; Bar-Or & Alexander 2016). As such, for small enough j, the NR coefficients dominate over the RR ones.

In order to evaluate the associated diffusion coefficient, $D^{\rm NR}_{jj}(a, j)$, we used the exact same approach as in Appendix C of Bar-Or & Alexander (2016). In a nutshell, the calculation proceeds as follows. (i) At a given phase-space location $(\mathbf{r}, \mathbf{v})$, one computes the local velocity diffusion coefficients, $\langle \delta \mathbf{v} \rangle(\mathbf{r}, \mathbf{v})$ and $\langle (\delta \mathbf{v})^2 \rangle(\mathbf{r}, \mathbf{v})$, see equation (7.83a) in Binney & Tremaine (2008). We note that here this calculation is greatly simplified by our assumption that the background cluster is fully relaxed, i.e. the cluster follows an isotropic DF, $F_{\rm tot} = F_{\rm tot}(E)$. (ii) The local diffusion coefficients are then translated into local diffusion coefficients in energy and angular momentum, e.g. $\langle \delta E \rangle(\mathbf{r}, \mathbf{v})$, $\langle \delta J \rangle(\mathbf{r}, \mathbf{v})$. (iii) These local kicks then accumulate as the star moves along its Keplerian wire. Following an orbit-average, one obtains therefore the associated orbit-averaged diffusion coefficients, e.g. $\langle \Delta J \rangle(a, j) = \oint \frac{{\rm d}M}{2\pi} \langle \delta J \rangle$. (iv) Having obtained the first- and second-order diffusion coefficients within the orbital coordinates (E, J), we can obtain the associated diffusion coefficients in the (a, j) space through the appropriate change of variables, in particular $\langle (\Delta j)^2 \rangle(a, j) = D^{\rm NR}_{jj}(a, j)$. In practice, we define the Coulomb logarithm of a family as $\ln \Lambda_i = \ln (M_\bullet / m_i)$ (see equation (7.84) of Binney & Tremaine 2008). Because they do not involve any resonance condition, these NR diffusion coefficients are numerically much less demanding to compute than the RR ones.

In Fig. 1, we also illustrate these NR diffusion coefficients. In practice, contrary to the RR ones, the NR diffusion coefficients are mostly independent of the stars' eccentricities. Finally, in Fig. 2 we illustrate the overall dependence of the total diffusion coefficients from equation (8), i.e. both the RR and NR contributions, in the whole (a, j) orbital space. In that figure, one can clearly note the presence of resonance lines associated with RR. One also notes that the bulk of the currently observed S-stars lie in a region of orbital space, where the diffusion of eccentricities is dominated by resonant effects. As a consequence, it is essential to account for these resonant mechanisms in order to accurately describe the dynamical fate of the S stars' eccentricities. One notes finally that the diffusion coefficient varies significantly as a function of j and stalls dramatically for $j \to 1$. As a result, it takes a much shorter amount of time for initially low eccentricity orbits to thermalize, or equivalently for a given age, it requires less massive unresolved perturbers (see also Fig. 3 below).

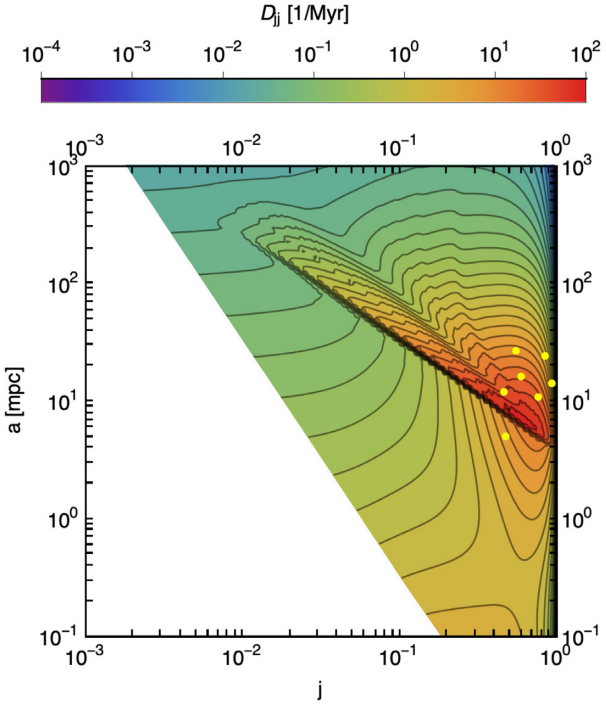

Figure 2. Illustration of the variation of the total diffusion coefficients, $D_{jj}(a, j)$, in orbital space (semimajor axis, a and eccentricity, j) for the Top-Heavy model (see section 3.1). Here are also represented in yellow all the S-stars (Gillessen et al. 2017), which were used to constrain the properties of the underlying unresolved stellar cluster. The white region on the left represent the location in orbital space of the central BH's loss cone. In the centre of the figure, resonant couplings in RR create this rugged but accurate aspect, that can be linked to that of the isocontours of the resonance frequencies, see Fig. A1.

3 APPLICATION

Having quantified the two main diffusion processes through which stars can relax in eccentricities in galactic nuclei, let us use them as dynamical probes in the context of the recent observation of the S-stars' eccentricities within SgrA*.

3.1 Model's assumption

For observational data, we use the orbital parameters listed in Gillessen et al. (2017). Specifically, we use the (a, j) coordinates for seven of those stars (S1, S2, S4, S6, S8, S9, S12). Indeed, for these stars, Habibi et al. (2017) provides us also with their main-sequence ages. These ages are a measure of the total time that the diffusion equation (5) has had to operate. For simplicity, we assume that on these time-scales, the NR of the S-stars' energies did not drive any significant diffusion, so that the stars' semimajor axes, a, are kept fixed. Regarding the initial conditions for the stars' eccentricities, we investigate two possible scenarios, either originating from binary tidal disruptions (Hills 1988; Gould & Quillen 2003; Alexander 2017), i.e. large initial eccentricities, or from an episode of disc formation (Alexander 2005; Levin 2006; Koposov et al. 2019), i.e. small initial eccentricities. In practice, we assume that the S-stars are initialized following a Gaussian distribution centred at $j(t = 0) = 0.2$ – with width 0.02 – to mimic the eccentricity distribution of binary disruptions (Generozov & Madigan 2020), or $j(t = 0) = 0.9$ to mimic *in-situ* disc formation. For alternative scenario, see also

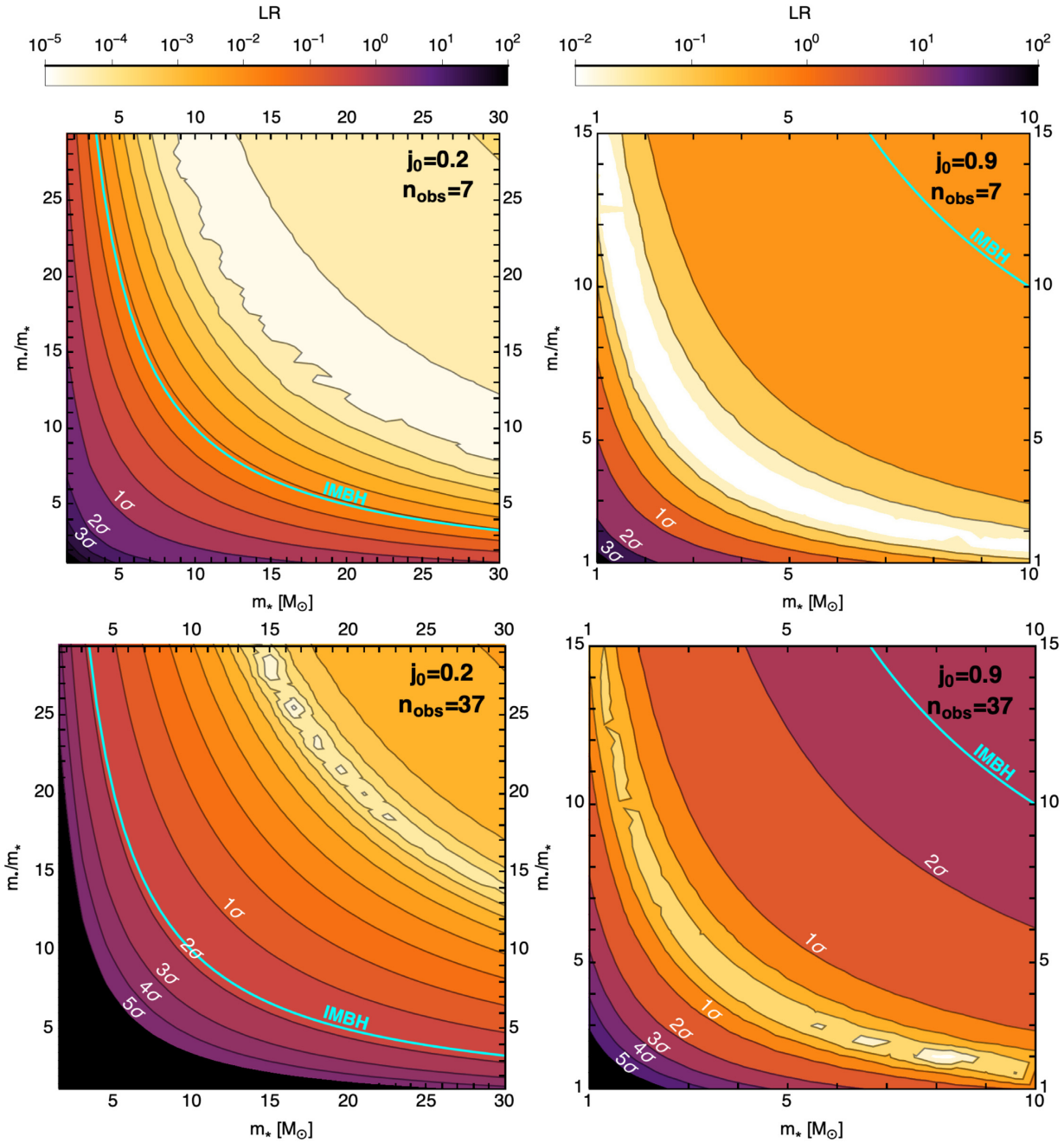

Figure 3. Confidence regions for the Top-Heavy model (see section 3.1) using the maximum-likelihood method applied to the observed S-stars, assuming a large initial eccentricity ($j_0 = 0.2$, the canonical value, left-hand panels), or a small initial eccentricity ($j_0 = 0.9$, right-hand panels). The cyan line corresponds to $m_\bullet = 100$ M$_\odot$, above which the heavy objects are usually considered as IMBHs. The cusp's indices and the total enclosed masses are fixed to their fiducial values (see equation 14), but we let the individual masses, ($m_\star$, $m_\bullet$), vary. Confidence levels are inferred from the LR test, see equation (17). The top panels only used the seven S-stars with known orbital parameters and stellar ages (Habibi et al. 2017), while the bottom ones expanded this observed sample using the other 30 S-stars (Gillessen et al. 2017), assuming a common age $T = 7.1$ Myr, i.e. the average age of the constrained seven S-stars. As expected, the smaller j_0, i.e. the more eccentric the stellar initial conditions, the slower the relaxation of the S-stars. Similarly, the larger the observed sample, the tighter the constraints on the background clusters.

Madigan, Levin & Hopman (2009), Perets, Hopman & Alexander (2007).

Let us also now make key assumptions regarding the background old stellar cluster. As detailed in Appendix B, we assume that it is composed of various subpopulations of different individual masses m_i with a total mass $M_i(<a_0)$ enclosed within a physical radius a_0. In addition, we also assume that each population follows a thermal distribution in eccentricity, and infinite power-law distribution in semimajor axes, that is,

$$M_i(<a) = M_i(<a_0)\left(\frac{a}{a_0}\right)^{3-\gamma_i}. \quad (13)$$

We also assume here that throughout their eccentricity diffusion, the S-stars are treated as test stars. As such, they do not contribute to the system's mean potential, and do not interact with one another.

Since we expect the background to be thermal, the RR dynamical friction vanishes exactly (Bar-Or & Fouvry 2018). Conversely, we also neglect the NR part of dynamical friction, since energy diffusion is inefficient in quasi-Keplerian systems on SRR time-scale (Bar-Or & Alexander 2016).

Assuming a two-family background composed of stars and another heavy subpopulation (e.g. IMBHs), we then have a total of 7 free parameters for the available models, namely the power indices ($\gamma_\star$, $\gamma_\bullet$), the individual masses ($m_\star$, $m_\bullet$), the total enclosed masses ($M_\star(< a_0)$, $M_\bullet(< a_0)$) as well as the initial eccentricity of the S-stars, $j_0 = j(t = 0)$. These models are complemented with the observed constraints on the seven considered S-stars, namely their main-sequence age, as well as their observed semimajor axis and eccentricity.

In practice, we started our investigation from the two-family Top-Heavy model of Generozov & Madigan (2020). Using $a_0 = 0.1$ pc, the fiducial model contains both stars and IMBHs

$$\begin{cases} m_\star &= 1\,\mathrm{M}_\odot, \\ m_\bullet &= 50\,\mathrm{M}_\odot, \end{cases} \begin{cases} M_\star(< a_0) &= 7.9\times10^3\,\mathrm{M}_\odot, \\ M_\bullet(< a_0) &= 38\times10^3\,\mathrm{M}_\odot, \end{cases} \begin{cases} \gamma_\star &= 1.5, \\ \gamma_\bullet &= 1.8, \end{cases} \tag{14}$$

where the star parameters follow Schödel et al. (2017). We note that such a model is compatible with the current constraints associated with S2's pericentre shift (Gravity Collaboration 2020), since $M_\bullet(< r_{\rm apo}^{\rm S2}) + M_\star(< r_{\rm apo}^{\rm S2}) \simeq 2500\,\mathrm{M}_\odot$.

3.2 Methodology

Having picked a set of initial conditions for the S-stars, and a model for the background clusters, we are now in a position to compute the associated diffusion coefficients. In order to determine whether or not such a model is compatible with the observational constraint of a significant eccentricity relaxation of the S-stars, we proceeded as follows.

We first compute the RR and NR diffusion coefficients for the a of the S-stars considered. The total diffusion coefficients are then interpolated and we integrate equation (5) forward in time using finite elements. More precisely, we rely on the so-called method-of-lines implemented in the `MathematicaNDSolve` function, which discretizes the j dimension and integrates the semidiscrete problem as a system of Cauchy's ODEs. As the semimajor axes are conserved, they can be integrated separately. As such, we integrate equation (5) for each of the seven considered S-stars, for a total time equal to the age of the star. In order to ensure that the PDF stays normalized during the integration, it is useful to rewrite equation (5) into

$$j^2\frac{\partial P}{\partial t} = \frac{j^2}{2}\frac{\partial}{\partial j}\left(D_{jj}\frac{\partial P}{\partial j}\right) - \frac{1}{2}\left[j\frac{\partial(D_{jj}P)}{\partial j}\right] + \frac{D_{jj}P}{2}, \tag{15}$$

in order to avoid the $1/j$ singularities. In practice, we also checked the sanity of this integration using stochastic Monte Carlo realizations, see Appendix D. Once these integrations performed, we compare the reached PDF to the observed data of the S-cluster, determining whether or not the background model allowed for an efficient enough relaxation of the S-stars eccentricities.

Let us denote a model with $\boldsymbol{\alpha}$, i.e. the collection of the seven parameters of the background clusters and the S-stars' initial eccentricities. We then define a model's likelihood as

$$L(\boldsymbol{\alpha}) = \prod_k P(j_k|a_k), \tag{16}$$

where $k = 1, ..., 7$ go through the seven S-stars mentioned before. Relying on equation (16), we can then explore the space of parameters $\boldsymbol{\alpha}$ and compare the various models to one another. To that end, we use the likelihood ratio (LR) test through

$$\lambda_R(\boldsymbol{\alpha}) = 2\ln\left(\frac{L_{\max}}{L(\boldsymbol{\alpha})}\right) \in [0, +\infty[, \tag{17}$$

When $\boldsymbol{\alpha}$ maximizes the likelihood, it minimizes by definition this likelihood ratio (as would a χ^2 analysis for Gaussian statistics), such that $\lambda_R(\boldsymbol{\alpha}) = 0$. Then, we can reject a model $\boldsymbol{\alpha}$ with confidence $0 \leq p \leq 1$, if the corresponding LR, $\lambda_R(\boldsymbol{\alpha})$, lies above a certain (explicit) value η_p. This is further detailed in Appendix E.

3.3 Results with existing data

As an illustration of the present method, we first consider the Top-Heavy model from equation (14), and let the individual masses $m_\star$ and $m_\bullet$ vary, with the natural constraint $m_\bullet \geq m_\star$ while fixing the total enclosed masses $M_\bullet(< a_0)$ and $M_\star(< a_0)$. This is presented in Fig. 3. In that figure, a model outside of the region of confidence $n\sigma$ means that it can be discarded with confidence $n\sigma$, as it would not allow the diffusion process to be fast enough to reach the observed eccentricity distribution of the S-cluster.

As expected, in Fig. 3 (top left-hand panel), we recover that the larger the individual masses, the larger the underlying Poisson shot noise, and therefore the more efficient the diffusion process, the faster the relaxation of the S-stars. Conversely, Fig. 3 shows that models with small individual masses cannot explain the current S-cluster's angular momentum PDF. As such, a relatively massive set of background sources orbiting within the S-cluster is required to trigger a fast enough orbital diffusion of the observed stars over their lifetime. Using the same data, in Fig. 3 (top right-hand panel), we also changed the initial eccentricity of the S-stars to $j_0 = 0.9$, to mimic an episode of disc formation. As already observed in Fig. 2, we note that the diffusion coefficient is larger at smaller eccentricities, so that the diffusion proceeds more swiftly, hence enhancing the overall efficiency of the relaxation of the S-stars.

The global shape of the likelihood contours presented in Fig. 3 clearly illustrates the known dynamical degeneracy in flipping IMBHs and stars of the same mass, as the efficiency of eccentricity relaxation is directly connected to the amplitude of the Poisson fluctuations generated by the background clusters as a whole. Interestingly, we note that all likelihood landscapes presented in the top panels present an absolute minimum. This suggests that, having only diffused a finite time, the observed eccentricity distribution of the S-stars is not fully thermal.

In order to increase the observed stellar sample, and tighten the inferred model constraints, we present in the bottom panels of Fig. 3 the same measurement but using 30 additional S-stars (as in fig. 13 of Gillessen et al. 2017). Their individual ages was fixed to $T = 7.1$ Myr, i.e. the average age of the seven S-stars whose ages have been measured (Habibi et al. 2017). As expected, we recover that a larger sample of observed stars leads to narrower contours around the likelihood extremum, making the presence of second population of massive objects all the more mandatory. Finally, we also note that since the expanded sample of 37 stars contains stars with semimajor axes larger than that of the initial seven S-stars, i.e. stars whose eccentricity relaxation is longer, the location of the likelihood maximum gets displaced to larger masses as one increases the observed stellar sample.

3.4 Prospective

Let us now carry out an experiment where we vary the number of stars for which orbital parameters are available, i.e. a prospective experiment appropriate for future surveys (Do et al. 2019).

We consider a similar model as the one in equation (14) where we set $m_\star = 5\ \mathrm{M}_\odot$ and $m_\bullet = 20\ \mathrm{M}_\odot$. We now wish to probe how the number of observed stars impacts our constraints on the determination of the background cluster parameters. To that end, we take the same seven S-stars as in Fig. 3, and consider their semimajor axes and main-sequence ages. For each of the seven semimajor axes, we evolve the PDF from equation (5) from $j_0 = 0.2$ for the entire star's observed lifetime. From the resulting PDFs, we draw N stars for each semimajor axis. In total, we therefore assume that our observation sample is composed of a total of $n_{\rm obs} = 7N$ stars. This sample constitutes our mock data, to which we apply the previous likelihood analysis.

Following this approach, Fig. 4 shows the ability of the method to constrain the parameters of the IMBH population given a larger mock sample. While the stellar parameters $(m_\star, \gamma_\star)$ are observables, we illustrate in that figure how the maximum-likelihood approach indeed allows us to constrain the parameters of the invisible dark cluster $(m_\bullet, \gamma_\bullet)$, that cannot be directly observed. As $(m_\bullet, \gamma_\bullet)$ are not degenerate with one another, an increase in the number of measured eccentricities (from $N = 1$ to $N = 100$ from top to bottom panels) narrows the confidence contours around the extremum of the likelihood, which itself converges to a specific pair $(m_\bullet, \gamma_\bullet)$ close to the fiducial one (green dot).

We further pursue this experiment in Fig. 5, where we investigate the expected improvements in the inferred constraints as a function of the number of observed stars, $n_{\rm obs}$. For a given mock realization, we compute the uncertainty $\sigma_{m_\bullet}$, defined as the width of the LR w.r.t. $m_\bullet$ at the 3σ height and fixed $\gamma_\bullet = 1.8$. This is represented in Fig. 5 as a function of $n_{\rm obs}$. Since the maximum-likelihood estimator is asymptotically normal and efficient (see e.g. Wasserman 2004) it reaches the Cramér–Rao bound in the large $n_{\rm obs}$ limit, so that $\sigma_{m_\bullet}(n_{\rm obs}) = \sigma_3/\sqrt{n_{\rm obs}}$, with $\sigma_3 \simeq 220\ \mathrm{M}_\odot$. Assuming crudely that the number of resolved stellar orbits is proportional to the survey's bolometric limit, one can directly connect a target accuracy with the survey's limiting magnitude. Indeed, the survey's magnitude would simply read $M = -2.5\log_{10}[(\sigma_{m_\bullet}/\sigma_3)^{-2}]$. Gaining a factor two in the accuracy of the mass (i.e. $\sigma_{m_\bullet} \to \sigma_{m_\bullet}/2$) would require a survey that is at least $\Delta M = -5\log_{10}(2) \simeq -1.5$ magnitudes fainter. Undoubtedly, upcoming surveys of SgrA*'s stellar neighbourhood, such as GRAVITY+ (Eisenhauer 2019; Gravity Collaboration 2021), TMT (Do et al. 2019), and ELT/MICADO (Davies et al. 2018; Pott et al. 2018) are on the verge of putting ever more stringent dynamical constraints on the unresolved dark cluster. Indeed, the central stellar cusp around SgrA* is strongly confusion-limited for current observations on 8 m class telescopes with adaptative optics, limiting in effect the reliable detection and measurement of positions of stars to K magnitudes ∼16–17.5, i.e. main-sequence B stars. The combination of MICADO and the ELT will push the effective stellar detection sensitivity by $\gtrsim$5 magnitudes with modest integration times (Fiorentino et al. 2019).

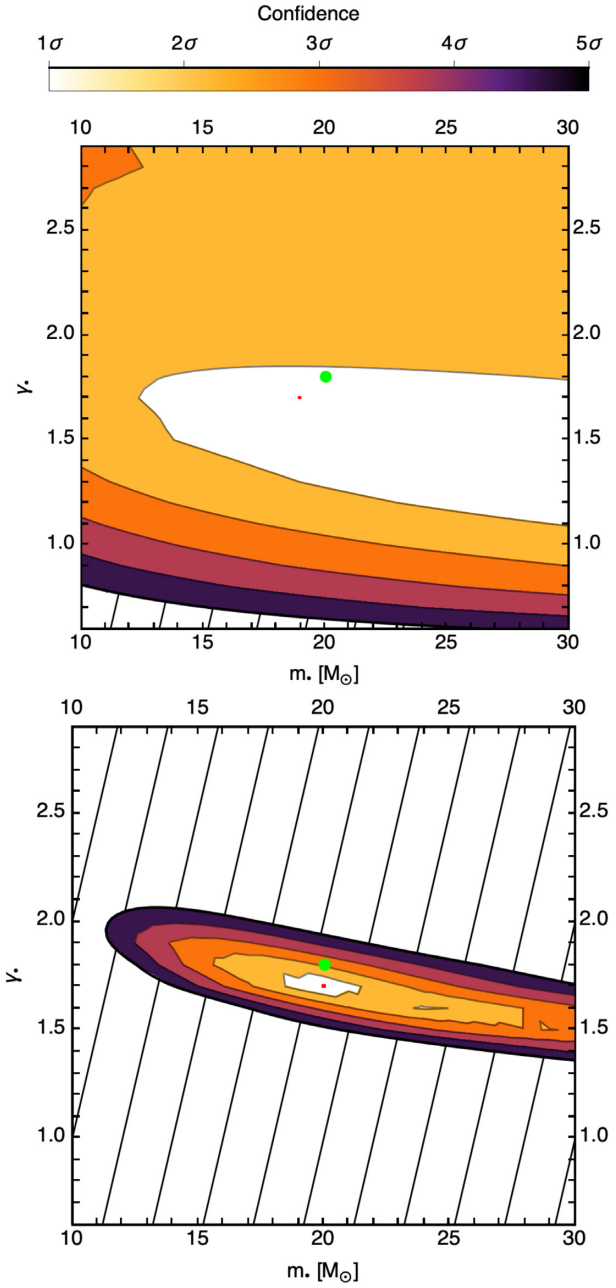

Figure 4. Same analysis as in Fig. 3, but applied to mock data, as detailed in section 3.4, as one varies the parameters, $(m_\bullet, \gamma_\bullet)$, of the IMBH population (keeping the total enclosed mass fixed). The top panel corresponds to mock data with $n_{\rm obs} = 7$ stars, while the bottom panel uses $n_{\rm obs} = 700$ stars. As expected, increasing the observed sample narrows the confidence contours around the maximum-likelihood estimator (red dot), which converge towards the fiducial model (green dot).

4 DISCUSSION AND CONCLUSION

In the spirit of Generozov & Madigan (2020), this paper was an attempt at using kinetic theory and its dynamical diagnostics to assess the structure of galactic nuclei. We showed how eccentricity diffusion in galactic nuclei can be used to place constraints on the stellar and putative dark clusters present therein. The recent observations of the (quasi-) thermal distribution of eccentricities of the S-stars orbiting SgrA*, in conjunction with updated computations of the eccentricity diffusion coefficients, can now be leveraged to this purpose. Investigating a simple two-populations model (see section 3.1), we showed how the presence of a heavy sub-population, e.g. IMBHs, is mandatory to source an efficient enough relaxation of the S-stars' eccentricities. We jointly showed how only some ranges of dark cusp's power-law indices and masses are compatible with that

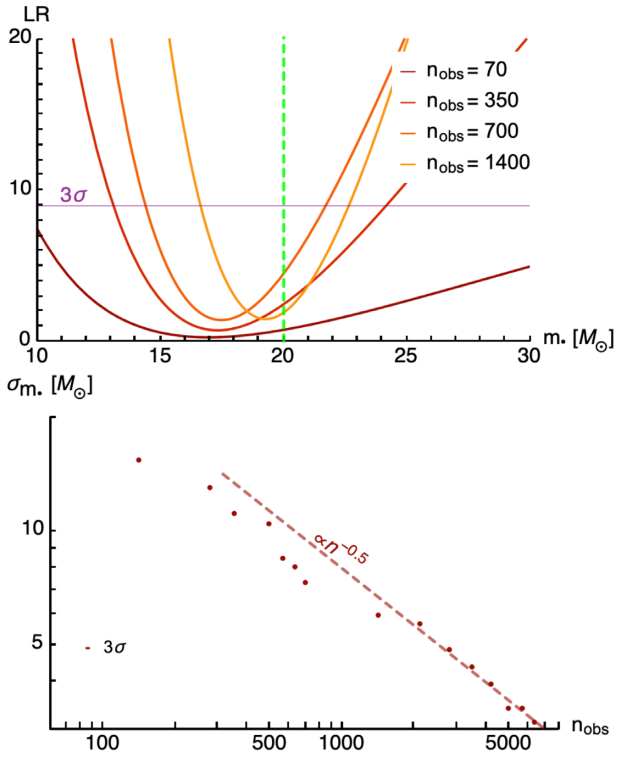

Figure 5. Same as in Fig. 4, using the same mock data, but with varying numbers of observed stars, $n_{\rm obs}$. The top panel shows the evolution of the LR at fixed $\gamma_\bullet = 1.8$, as a function of $m_\bullet$, for various values of $n_{\rm obs}$. The vertical green line represents the fiducial parameters model, $m_\bullet = 20$ M$_\odot$. The horizontal line represents the value of the LR for a 3σ confidence contour. The bottom panel illustrates the evolution of the accuracy, $\sigma_{m_\bullet}$, of the inferred IMBH mass as a function of the $n_{\rm obs}$, and for the 3σ confidence levels. For the modified TopHeavy model we use, we expect $\sim 10^3$ stars within 5 and 20 mpc. Of course we do not expect to observe so many stars around SgrA*, i.e. the asymptote $1/\sqrt{n_{\rm obs}}$ will not be attained, because of crowding and, more importantly, because the total number of observed S-stars will be much smaller than 5000.

same dynamical constraint. As expected, our analysis highlighted intrinsic dynamical degeneracies in permuting the visible and dark cluster. Assuming that upcoming experiments will better qualify the properties of the visible cluster, kinetic theory will allow for dynamical dark matter experiment to constrain both the typical mass and geometry of the IMBH cluster.

Finally, a simple fiducial experiment allowed us to quantify the depth that upcoming surveys should achieve in order to e.g. double the accuracy on the IMBH's mass required to match the data. More generally, this investigation suggests that it will be of interest to lift some of the degeneracies by increasing the number of measured stellar ages, better quantify the mass function and shape of the observed stellar cluster and initial eccentricity distribution, so that kinematic modelling can further focus on dynamically quantifying the properties of the dark cluster.

4.1 Perspectives

Let us now discuss some venues for future developments. As shown in section 3.1, the present investigation relies on various assumptions, some of which one could hope to partially lift. Our models for the old stellar and dark cluster remain simplistic, and it will be worthwhile to investigate possible contributions from other populations such as a dark-matter dominated components, or additional populations of IMBHs. Similarly, as already emphasized in equation (5), we assumed that the background cluster is spherically symmetric. Yet, Szölgyén & Kocsis (2018) recently showed that in systems with a large mass spectrum, e.g. containing IMBHs, one could expect VRR to lead to equilibria distribution where the massive components follow a strongly anisotropic structure, i.e. aligned within the same disc. Such a structure could definitely affect the efficiency of eccentricity relaxation within it. Any additional non-trivial structures present in that PDF, e.g. non-spherically symmetric distributions or dearth of stars in orbital space, would also have to be explained by the present diffusion processes. Similarly, on scales even closer to the central BH, we would also have to account for additional relativistic corrections stemming from it, e.g. effects associated with its spin.

Observations show that 7–10 per cent of the stars may have originated from an infalling population. These stars display significant rotation (Do et al. 2020) and likely populate a disc. The most direct impact of that disc would be to induce mean-field torquing on the orbital planes, but it might also impact later on the eccentricities within the cluster. Recently, Szölgyén, Máthé & Kocsis (2021) have investigated this effect numerically and found that the time-scale for the eccentricity decrease is much shorter than Chandrasekhar's dynamical friction time-scale. This supports previous findings by Madigan & Levin (2012) that resonant dynamical friction, driven by orbit-averaged torques, dominates over ordinary non-resonant dynamical friction, driven by nearby encounters, and leads to eccentricity decrease for a corotating disc. From an analytical perspective, a possible venue would be to revisit the present kinetic theory, while relying on a Stäckel description of the cluster's density, so as to keep it integrable and account for its flattening. This would clearly be an order of magnitude more complicated than the path chosen in this paper, as it would increase the dimension of action space to be considered, as well as require one to use elliptic coordinates (even the linear-response of flattened systems has scarcely been investigated in the literature; Robijn 1995).

We emphasize that the mass in the S-star cluster is only a small fraction of the total enclosed mass within 1 arcsec of the central black hole. As such, it is unlikely that the S cluster itself strongly disturbs the background stellar distribution. We also assumed here that this background cluster was thermal ($F(j) = 2j$) hence fully relaxed. In that limit, it does not drive any RR dynamical friction (Bar-Or & Fouvry 2018). Should we lift this assumption, a more accurate modelling would include the coupling between both components of the cluster as a two-populations model. This would require integrating the coupled set of kinetic equations in time, rather than relying on a frozen Fokker–Planck approximation for the diffusion coefficient. While this might be a worthwhile endeavour for upcoming data sets, it is clearly beyond the scope of this first investigation.

When modelling the S-stars' dynamics, we assumed that the semimajor axes of the stars were fixed throughout the diffusion, owing to the orbit-average. While accounting for the contributions from the NR diffusion coefficients in a, it could be interesting to investigate whether any additional diffusion in a-space would affect the present constraints. As already noted, the initial conditions of the S-stars, e.g. very eccentric versus quasi-circular, strongly affect the efficiency of their eccentricity relaxation (see Fig. 3). In particular, one can expect that the distribution of the S-stars in semimajor axes also carries some information on their initial formation mechanism.

Here, we focused our interest on the innermost S-stars ($a \simeq 5$ mpc), which are known to have partially relaxed in eccentricity. This allowed us to place constraints on cluster models so

that admissible clusters have to source an eccentricity diffusion that is fast enough. One could use a similar approach to investigate the relaxation of S-stars further out. These outer stars have only very partially relaxed in eccentricity, so that any admissible cluster model must source a diffusion that is slow enough for these outer regions not to have fully relaxed. Leveraging both constraints, one should be in a position to effectively bracket cluster models, given that their induced diffusion must be both efficient enough in the inner regions, and inefficient enough in the outer ones. A same double-sided investigation could also be carried out in the context of the VRR of the same S-stars, as it has been observed that the innermost stars follow a spherically symmetric distribution, while the outer ones tend to be aligned within a disc (Bartko et al. 2009; Yelda et al. 2014), i.e. orientation neighbours have not been separated (Giral Martínez, Fouvry & Pichon 2020). Once again, simultaneously accounting for all these dynamical constraints will allow for better characterizations of SgrA*'s dark and visible structures.

Finally, future observations will undoubtedly prove useful in placing these investigations on firmer grounds. First, the interferometer GRAVITY is currently tracking in details the trajectory of S2 (Gravity Collaboration 2020). Any deviations of its orbit from S2's expected mean-field trajectory, i.e. the expected Keplerian dynamics and in-plane precession, will bear imprints from the fluctuations of the gravitational potential on the scale of S2's orbit, that kinetic theory should be able to describe. Similarly, a possible observation from GRAVITY of stars on scales even smaller than S2 would also carry essential information on SgrA*'s stellar structure on smaller scales, i.e. closer to the central BH. On larger scales, one expects that observations from upcoming thirty-metre telescopes (Do et al. 2019) will allow for a finer characterization of the S-stars current distribution, $P(a, j, t)$, a very valuable dynamical information as shown in section 3.4. In particular, the dependence of P w.r.t. a is strongly dependent on the formation mechanism of these stars. Regarding the dependence w.r.t. j, one could in particular hope to measure the scale, i.e. the a, at which the S-stars diffuse less and less efficiently towards a thermal distribution of eccentricities, hence strongly constraining the efficiency of the diffusion mechanisms. We note that the present maximum-likelihood formalism can naturally be extended to account for the measurement uncertainties, such as on stellar ages.

Eventually, this line of investigation should prove useful in constraining supermassive black hole formation scenarios.

DATA DISTRIBUTION

The data underlying this article is available through reasonable request to the author. The code is distributed on github at the following URL: https://github.com/KerwannTEP/JuDOKA.

ACKNOWLEDGEMENTS

This work is partially supported by grant Segal ANR-19-CE31-0017 of the French Agence Nationale de la Recherche, and by the Idex Sorbonne Université. We thank Stéphane Rouberol for the smooth running of the Horizon Cluster, where the simulations were performed. CP thanks Renaud Foy, Fabien Malbet, and Eric Thiébaut for (very) early discussions about this project.

REFERENCES

Abbott B. P. et al., 2019, Phys. Rev. X, 9, 031040
Alexander T., 2005, Phys. Rep., 419, 65
Alexander T., 2017, ARA&A, 55, 17
Antonini F., Merritt D., 2012, ApJ, 763, L10
Bahcall J. N., Wolf R. A., 1976, ApJ, 209, 214
Bar-Or B., Alexander T., 2016, ApJ, 820, 129
Bar-Or B., Fouvry J.-B., 2018, ApJ, 860, L23
Bar-Or B., Kupi G., Alexander T., 2013, ApJ, 764, 52
Bartko H. et al., 2009, ApJ, 697, 1741
Binney J., Tremaine S., 2008, Galactic Dynamics, 2nd edn. Princeton Univ. Press, Princeton
Davies R. et al., 2018, in Evans C. J., Simard L., Takami H., eds, Proc. SPIE Conf. Ser. Vol. 10702, Ground-based and Airborne Instrumentation for Astronomy VII. SPIE, Bellingham, p. 107021S
Do T. et al., 2019, Bull. Am. Astron. Soc., 51, 530
Do T. et al., 2020, ApJ, 901, L28
Eisenhauer F., 2019, The Very Large Telescope in 2030, ESO Garching presentation
Event Horizon Telescope Collaboration 2019, ApJ, 875, L1
Fiorentino G. et al., 2019, preprint (arXiv:1712.04222)
Fouvry J.-B., Bar-Or B., Chavanis P.-H., 2019, ApJ, 883, 161
Fouvry J.-B., Dehnen W., Tremaine S., Bar-Or B., 2020, AAS, preprint (arXiv:2011.01673)
Generozov A., Madigan A.-M., 2020, ApJ, 896, 137
Ghez A. M. et al., 2008, ApJ, 689, 1044
Gillessen S. et al., 2017, ApJ, 837, 30
Giral Martínez J., Fouvry J.-B., Pichon C., 2020, MNRAS, 499, 2714
Gould A., Quillen A. C., 2003, ApJ, 592, 935
Gravity Collaboration 2017, A&A, 602, A94
Gravity Collaboration 2020, A&A, 636, L5
Gravity Collaboration 2021, A&A, 645, A127
Habibi M. et al., 2017, ApJ, 847, 120
Hills J. G., 1988, Nature, 331, 687
Hopman C., Alexander T., 2006, J. Phys. Conf. Ser., 54, 321
Kocsis B., Tremaine S., 2011, MNRAS, 412, 187
Kocsis B., Tremaine S., 2015, MNRAS, 448, 3265
Koposov S. E. et al., 2019, MNRAS, 491, 2465
Levin Y., 2006, MNRAS, 374, 515
Lightman A. P., Shapiro S. L., 1977, ApJ, 211, 244
Madigan A.-M., Levin Y., 2012, ApJ, 754, 42
Madigan A.-M., Levin Y., Hopman C., 2009, ApJ, 697, L44
Merritt D., 2013, Dynamics and Evolution of Galactic Nuclei. Princeton Univ. Press, Princeton
Merritt D., Gualandris A., Mikkola S., 2009, ApJ, 693, L35
Merritt D., Alexander T., Mikkola S., Will C. M., 2011, Phys. Rev. D, 84, 044024
Murchikova E. M., Phinney E. S., Pancoast A., Blandford R. D., 2019, Nature, 570, 83
Murray C., Dermott S., 1999, Solar System Dynamics. Cambridge Univ. Press, Cambridge
Perets H. B., Hopman C., Alexander T., 2007, ApJ, 656, 709
Portegies Zwart S. F., McMillan S. L. W., 2002, ApJ, 576, 899
Pott J. U. et al., 2018, in Evans C. J., Simard L., Takami H., eds, Proc. SPIE Conf. Ser. Vol. 10702, Ground-based and Airborne Instrumentation for Astronomy VII. SPIE, Bellingham, p. 1070290
Rauch K. P., Tremaine S., 1996, New A, 1, 149
Risken H., 1989, The Fokker-Planck Equation. Springer, Berlin
Robijn F. H. A., 1995, PhD thesis, Leiden Observatory
Schödel R. et al., 2017, A&A, 609, A27
Sridhar S., Touma J. R., 2016, MNRAS, 458, 4143
Szölgyén Á., Kocsis B., 2018, Phys. Rev. Lett., 121, 101101
Szölgyén Á., Máthé G., Kocsis B., 2021, ApJ, preprint (arXiv:2103.14042)
Touma J. R., Tremaine S., Kazandjian M. V., 2009, MNRAS, 394, 1085
Trefethen L. N., Weideman J. A. C., 2014, SIAM Rev., 56, 385
Vasiliev E., 2017, ApJ, 848, 10
Wasserman L., 2004, All of Statistics: A Concise Course in Statistical Inference. Springer, New York
Wilks S. S., 1938, Ann. Math. Stat., 9, 60
Yelda S. et al., 2014, ApJ, 783, 131

APPENDIX A: FREQUENCIES AND RESONANCES

In the vicinity of a supermassive BH, Keplerian wires undergo an in-plane precession of their pericentres, as described by equation (3). In that relation, the relativistic precession is given by

$$\nu_{\rm GR}(a,\,j) = 3\frac{r_{\rm g}}{a}\frac{1}{j^2}\nu_{\rm Kep}(a), \tag{A1}$$

where we introduced the (fast) Keplerian frequency, $\nu_{\rm Kep}(a)$, in equation (2), as well as the gravitational radius $r_{\rm g} = GM_\bullet/c^2$. In practice, this precession is said to be prograde as one always has $\nu_{\rm GR}(a,\,j) > 0$. The gravitational radius allows us to introduce a maximal eccentricity

$$j_{\rm lc}(a) = 4\sqrt{\frac{r_{\rm g}}{a}}, \tag{A2}$$

so that wires with $j \leq j_{\rm lc}(a)$ are assumed to be within the loss-cone (Merritt 2013), and, as such, are unavoidably absorbed by the central BH.

In order to easily compute $\nu_{\rm M}(a,j)$, the mass precession frequency imposed by the background stellar cluster, we assume that the stellar cluster follows an infinite power-law distribution of the form $M(<a) \propto a^{3-\gamma}$, where $M(<a)$ stands for the total stellar mass physically enclosed within the radius a. In that limit, following Appendix A of Kocsis & Tremaine (2015), the mass precession frequency reads

$$\nu_{\rm M}(a,\,j) = \overline{\nu}_{\rm M}(a)\,h_{\rm M}(j), \tag{A3}$$

where in that expression, the dimensional dependence w.r.t. a is captured by

$$\overline{\nu}_{\rm M}(a) = \nu_{\rm Kep}(a)\,\frac{M(<a)}{M_\bullet}, \tag{A4}$$

while the dimensionless eccentricity dependence is given by

$$h_{\rm M}(j) = \frac{j^{4-\gamma}}{1-j^2}\left[P_{1-\gamma}(1/j) - \frac{1}{j}P_{2-\gamma}(1/j)\right], \tag{A5}$$

with P_α the Legendre function of order α. In practice, near the edge $j = 1$, we note that $h_{\rm M}(j)$ can be advantageously replaced with its Taylor expansion

$$h_{\rm M}(j) \simeq \frac{1}{2}(-3+\gamma) - \frac{1}{8}(-12+\gamma+4\gamma^2-\gamma^3)(1-j), \tag{A6}$$

to avoid singularities.

Importantly, we note that the function $h_{\rm M}(j)$ is always negative for $\gamma < 3$. Indeed, following equation (A2) of Kocsis & Tremaine (2015), we can rewrite equation (A5) with the alternative integral form

$$\begin{aligned} h_{\rm M}(j) &= \frac{j^{2(3-\gamma)}}{\pi\sqrt{1-j^2}}\int_0^\pi {\rm d}\psi\,\frac{\cos(\psi)}{(1+e\cos(\psi))^{3-\gamma}}\,, \\ &= \frac{j^{2(3-\gamma)}}{\pi\sqrt{1-j^2}}\int_0^{\pi/2} {\rm d}\psi\,\cos(\psi) \\ &\quad\times\left\{\frac{1}{(1+e\cos(\psi))^{3-\gamma}} - \frac{1}{(1-e\cos(\psi))^{3-\gamma}}\right\}, \end{aligned} \tag{A7}$$

which is explicitly negative for any potential satisfying $3-\gamma > 0$. As a consequence, the mass precession is generically retrograde, i.e. one has $\nu_{\rm M}(a,\,j) \leq 0$.

Fig. A1 illustrates the behaviour of the total precession frequency, $\nu_{\rm p}(a,\,j)$, as a function of the wire's underlying orbital parameters. Lines of constant precession frequencies correspond to the resonant lines along which the RR diffusion coefficients from equation (9) must be computed. Note that the precession of very eccentric orbits is dominated by the diverging relativistic corrections. This is responsible for the 'Schwarzschild barrier' (Merritt et al. 2011; Bar-Or & Alexander 2016) that explains the drastic reduction of the RR diffusion coefficients, shown in Fig. 1.

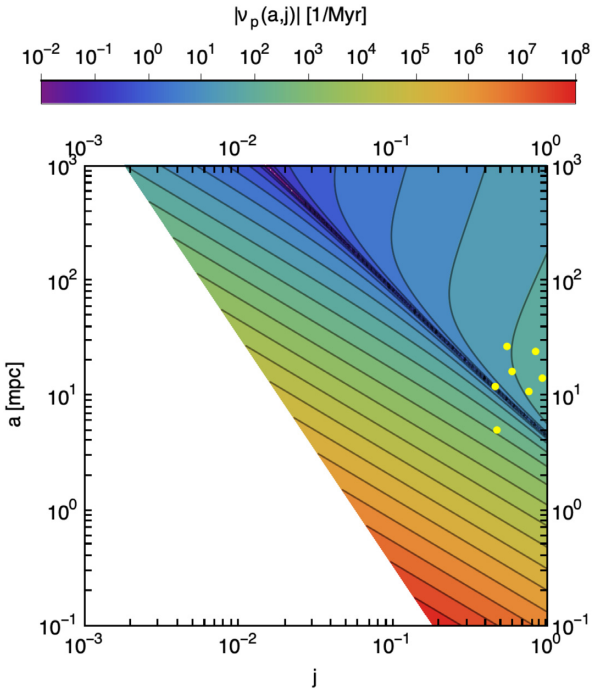

Figure A1. Illustration of precession frequencies, $|\nu_{\rm p}(a,j)|$, in orbital space for the model from Fig. 2. The orbital space locations of the seven S-stars used in our analysis are represented in yellow. For circular orbits and large semimajor axis, i.e. $j \to 1$ and $a \gg 1$ the precession is dominated by the mass precession and is therefore retrograde ($\nu_{\rm p} < 0$), while for low j and low a, the precession is dominated by the relativistic precession and is therefore prograde ($\nu_{\rm p} > 0$).

In order to compute the resonant diffusion coefficients from equation (9), we must solve the resonance condition from equation (10). For a given wire (a,j), and a given resonance pair (n,n'), this involves characterizing all the wires (a',j') such that $n'\nu_{\rm p}(a',j') = n\nu_{\rm p}(a,j)$, i.e. identifying the appropriate level lines in Fig. A1. In Fig. A2, we illustrate the contributions from the various resonance pairs (n,n') to the total RR diffusion coefficients.

Let us briefly detail our implementation for the search of the resonant lines. Here, the key remark is to note that, following equations (A1) and (A5), one always has ${\rm d}\nu_{\rm p}/{\rm d}j < 0$. As a consequence, for a given value of a', it is straightforward to determine whether or not there exists a j', with $j_{\rm lc}(a') \leq j' \leq 1$, and $n'\nu_{\rm p}(a',j') = n\nu_{\rm p}(a,j)$. Using this approach, we may then identify a domain $a'_{\rm min} \leq a' \leq a'_{\rm max}$, within which the resonance condition can be satisfied, by solving appropriately the resonance conditions along the critical lines $j = j_{\rm lc}(a)$ as well as $j = 1$. At this stage, we also enforce that $16\,r_{\rm g} \leq a'_{\rm min}$ (see equation A2) as well as $a'_{\rm max} \leq r_{\rm h}$, with $r_{\rm h}$ the considered influence radius (e.g. $r_{\rm h} = 2$pc for SgrA*), to ensure that we limit ourselves only to meaningful resonant regions of orbital space.

Once the range $[a'_{\rm min}, a'_{\rm max}]$ has been determined, to emphasize the system's partial scale-invariance, we sample this domain of semimajor axis linearly in log-space, using $K_{\rm res} = 100$ points. Finally, for a given value a' such that $a'_{\rm min} \leq a' \leq a'_{\rm max}$, the associated resonant value j' is directly obtained by bisection. For models with γ

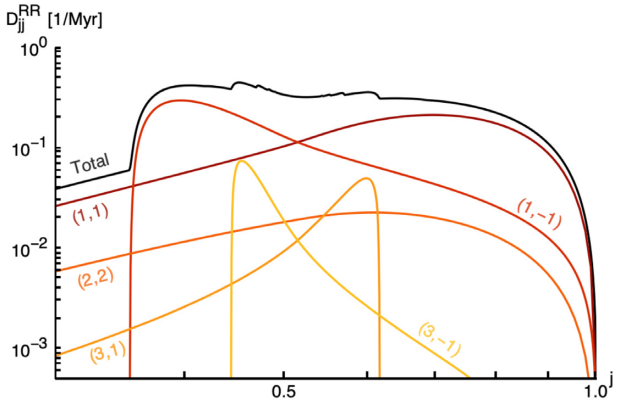

Figure A2. Illustration of the contribution to the RR diffusion coefficients of the different resonances (n, n'), for a given value semimajor axis $a = 10$ mpc and the cutoff $\ell_{\max} = 10$, for the model from equation (14). The RR coefficients are typically dominated by $(n, n') = (1, 1)$ (for small and large j) and $(n, n') = (1, -1)$ (for intermediate j). For intermediate eccentricities, higher order resonances also contribute.

< 1.5, it can happen that $a \mapsto \nu_p(a, j)$ is not monotonic anymore for j close to 1 (circular orbit), leading to the possible appearance of a second range of semimajor axes over which the resonance condition is satisfied. When this is the case, we accordingly sample this domain using the same method.

APPENDIX B: STELLAR CUSPS AROUND SGR A*

For the sake of simplicity, we assume that all the background populations follow infinite power-law distributions, which eases the resolution of the resonance condition (see Appendix A).

Let us first specify our conventions for the normalizations of their respective DFs. A given background population is characterized by four numbers, namely γ, the slope of the power-law profile, m, the individual mass of the stars, a_0, a given radius of reference, and $M(< a_0)$, the total stellar mass physically within the radius a_0. The number of stars per unit semimajor axis a is then given by

$$N(a) = (3-\gamma)\,\frac{N_0}{a_0}\left(\frac{a}{a_0}\right)^{2-\gamma}. \tag{B1}$$

In that expression, we introduced $N_0 = g(\gamma)N(< a_0)$ with

$$g(\gamma) = 2^{-\gamma}\,\sqrt{\pi}\,\frac{\Gamma(1+\gamma)}{\Gamma(\gamma-\frac{1}{2})}, \tag{B2}$$

where $N(< a_0) = M(< a_0)/m$ is the number of stars physically within a radius a_0. This number should not be confused with N_0 that is the number of stars with a semimajor axis smaller than a_0.

In addition, we also assume that each background population is thermally relaxed, so that, as in equation (11), we have

$$f(j|a) = 2j, \tag{B3}$$

which is the equilibrium solution of equation (5). When one accounts for the fact no wires can survive within the loss-cone, this thermal PDF gets truncated, and becomes

$$f(j|a) = \frac{2j}{1 - j_{\rm lc}^2(a)}, \tag{B4}$$

where the limit eccentricity, $j_{\rm lc}(a)$, is defined in equation (A2).

APPENDIX C: COUPLING COEFFICIENTS

Let us now detail how one can efficiently compute the coupling coefficients $K^{\ell}_{nn'}(a, j, a', j')$ from equation (12). When written explicitly, they read

$$K^{\ell}_{nn'} = \int_0^{2\pi} \frac{{\rm d}M}{2\pi}\,\frac{{\rm d}M'}{2\pi}\,\cos(nf)\,\cos(n'f')\,\frac{{\rm Min}[r, r']^{\ell}}{{\rm Max}[r, r']^{\ell+1}}, \tag{C1}$$

where M and M' stand for the mean anomalies of both orbits, and we shortened the notation $K^{\ell}_{nn'} = K^{\ell}_{nn'}(a, j, a', j')$.

First, we note that the function $r \mapsto r(M)$ is an even function, so that we can reduce the range of both angular integrals to $[0, \pi]$. Moreover, in order not to have to invert Kepler's equation of motion, it is more convenient to perform these integrals w.r.t. the true anomalies f and f'. In particular, the radius r is directly obtained from f through (Murray & Dermott 1999)

$$r = \frac{a(1-e^2)}{1 + e\cos(f)}, \tag{C2}$$

with the associated Jacobian

$$\frac{{\rm d}M}{{\rm d}f} = \frac{r^2}{a^2}\,\frac{1}{\sqrt{1-e^2}}. \tag{C3}$$

Following these modifications, we can rewrite equation (C1) as

$$K^{\ell}_{nn'} = \int_0^{\pi} \frac{{\rm d}f}{\pi}\,\frac{{\rm d}f'}{\pi}\,\frac{{\rm d}M}{{\rm d}f}\,\frac{{\rm d}M'}{{\rm d}f'} \times \cos(nf)\,\cos(n'f')\,\frac{{\rm Min}[r, r']^{\ell}}{{\rm Max}[r, r']^{\ell+1}}. \tag{C4}$$

At this stage, a naive approach would be to discretize each integral into K discrete steps, and replace them with Riemann sums, accounting for a total complexity in $\mathcal{O}(K^2)$. Fortunately, dealing appropriately with the ratio of Min and Max, equation (C4) can be computed in $\mathcal{O}(K)$ operations, as these integrals are almost separable.

First, we sample uniformly the integration intervals from equation (C4) using K nodes. Specifically, we sample the true anomaly with

$$f_k = \Delta f\,\left(k - \frac{1}{2}\right), \quad \text{with} \quad 1 \le k \le K, \tag{C5}$$

where we introduced the step distance $\Delta f = \pi/K$. Here, following the midpoint-rule, each sampling location is offset by a factor $\frac{1}{2}$. This ensures that the 2π-periodic integrand is sampled uniformly, which allows for fast convergence of the result (Trefethen & Weideman 2014). Following this discretization, equation (C4) becomes

$$K^{\ell}_{nn'} = \frac{1}{K^2}\sum_{i,j} g_i\,g'_j\,\frac{{\rm Min}[r_i, r'_j]^{\ell}}{{\rm Max}[r_i, r'_j]^{\ell+1}}, \tag{C6}$$

where we introduced the function $g(r) = \cos(nf)\,{\rm d}M/{\rm d}f$, as well as the shorthand notations $g_i = g(r_i)$ and $g'_j = g(r'_j)$. One can now use the particular structure of equation (C6) to drastically accelerate its evaluation. To do so, we order the set of radii $\{r_i, r'_j\}$ by increasing order. We note that this can be done in $\mathcal{O}(K)$ steps, provided that the two sets $\{r_i\}$ and $\{r'_j\}$ are already ordered, so that it only remains to merge the two lists.

Following this sorting, we can now construct the array w_j which, for $1 \le j \le K$, is defined as

$$w_j = {\rm Card}\{i \in \{1, .., K\} | r_i \le r'_j\}, \tag{C7}$$

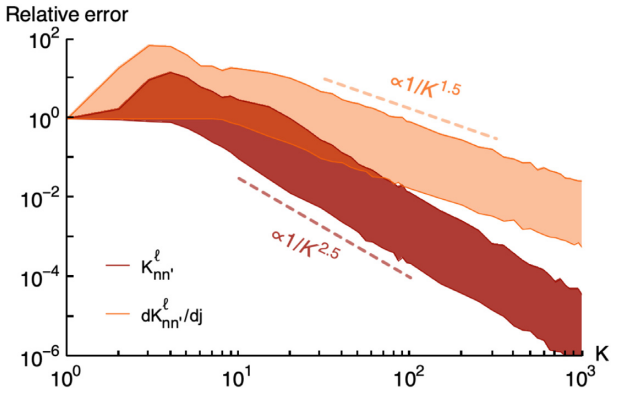

Figure C1. Illustration of the relative errors in the computations of $K^{\ell}_{nn'}$ (in brown) and $\mathrm{d}K^{\ell}_{nn'}/\mathrm{d}j$ (in orange) using the multipole approach from equation (C8), as a function of the number of nodes K. We approximated the real value by that obtained for $K = 2000$. The plotted regions represent the errors within the 16 and the 84 percentiles. The use of a mid-point rule allows for a fast convergence, though the regularity of the integrand does not allow for an exponential one. Errors are found to scale like $K \propto 1/K^{2.5}$ for $K^{\ell}_{nn'}$ and $K \propto 1/K^{1.5}$ for $\mathrm{d}K^{\ell}_{nn'}/\mathrm{d}j$. In practice, we use $K = 100$ to compute $K^{\ell}_{nn'}$, with a relative error smaller than 1 per cent.

with the boundary terms $w_0 = 0$ and $w_{K+1} = K$. The double sum from equation (C6) can then be rewritten as

$$K^{\ell}_{nn'} = \frac{1}{K^2}\sum_{j=1}^{K} g'_j[P_j + Q_j]. \tag{C8}$$

In that expression, we introduced the reduced sums P_j and Q_j that read

$$P_j = \sum_{i=1}^{w_j} g_i \frac{r_i^{\ell}}{r_j'^{\ell+1}}; \quad Q_j = \sum_{i=w_j+1}^{K} g_i \frac{r_j'^{\ell}}{r_i^{\ell+1}}. \tag{C9}$$

The key property here is note that the sum P_j (resp. Q_j) can be computed in $\mathcal{O}(K)$ through an increasing (resp. decreasing) recurrence. In order to highlight this property, we define the partial sums

$$\delta P_j = \sum_{i=w_{j-1}+1}^{w_j} g_i \frac{r_i^{\ell}}{r_j'^{\ell+1}}; \quad \delta Q_j = \sum_{i=w_j+1}^{w_{j+1}} g_i \frac{r_j'^{\ell}}{r_i^{\ell+1}}. \tag{C10}$$

The sums P and Q then satisfy the recurrence relations

$$P_1 = \delta P_1; \quad P_{j+1} = \left[\frac{r'_j}{r'_{j+1}}\right]^{\ell+1} P_j + \delta P_{j+1},$$
$$Q_K = \delta Q_K; \quad Q_{j-1} = \left[\frac{r'_{j-1}}{r'_j}\right]^{\ell} Q_j + \delta Q_{j-1}. \tag{C11}$$

Hence, given these two recurrence relations, equation (C8) can be computed in $\mathcal{O}(K)$ operations. Moreover, we note that the geometric prefactors appearing in equation (C11) are positive and always smaller than 1, which helps ensuring the numerical stability of these recurrences. In order to illustrate the quality of this discretization scheme, we present in Fig. C1 the behaviour of the relative error in the computation of $K^{\ell}_{nn'}$ as a function of K. The relative errors appears to scale like $1/K^{2.5}$. From this observation, we can infer that $K = 100$ is enough to obtain a 1 per cent relative error for any orbital parameter.

Following equation (7), we note that the computation of the first-order diffusion coefficient ultimately also requires the computation of $\mathrm{d}K^{\ell}_{nn'}/\mathrm{d}j$. It is straightforward to extend the previous recurrence relations to compute such a derivative. In Fig. C1, we also illustrate the typical relative error in the computation of $\mathrm{d}K^{\ell}_{nn'}/\mathrm{d}j$. In particular, we note that this gradient introduces discontinuities in the integrand, which reduces the convergence speed of the method to an inverse power law proportional to $1/K^{1.5}$.

Table C1. Computation time of $D^{\mathrm{RR}}_{jj}(a, j)$ for $a = 10$ mpc, $j = 0.6$ and for the same Top-Heavy model as in Fig. 2. Fixing $\ell_{\max} = 10$, we observe a linear complexity w.r.t. K (second line), while fixing $K = 100$, we observe a complexity in $(\ell_{\max})^{2.3}$ w.r.t. $\ell_{\max}$.

K	20	40	60	80	100	150	200	250
Time (s)	0.51	0.72	0.96	1.13	1.30	1.89	2.44	2.96
$\ell_{\max}$	6	8	10	12	14	16	18	20
Time (s)	0.38	0.76	1.35	2.12	2.93	4.16	5.54	7.72

With such an approach, we expect that computing the diffusion coefficient D^{RR}_{jj} should have a complexity linear w.r.t. K, as recovered in Table C1. Finally, the complexity of the computation of D^{RR}_{j} w.r.t. $\ell_{\max}$ follows a power law roughly proportionnal $(\ell_{\max})^{2.3}$. Such a scaling is primarily due to the growth of the number of resonance pairs (n, n') as $\ell_{\max}$ increases.

APPENDIX D: SIMULATING STOCHASTIC DYNAMICS

One approach to simulate the relaxation of the test stars' eccentricities is to rely on Monte Carlo realizations of the underlying diffusion equation. This is more easily done starting from the traditional form of the FP equation, as given by equation (6), which involves the first- and second-order diffusion coefficients. We used this alternative approach to check the validity of our direct numerical integration of the diffusion equation (5).

Following Risken (1989), one can mimic the dynamics of a given test star through the stochastic Langevin equation

$$\Delta j = D_j\,\Delta t + \sqrt{D_{jj}\,\Delta t}\,\xi(t). \tag{D1}$$

In that expression, Δt is our chosen (fixed) time-step, and $\xi(t)$ follows a normal distribution of unit variance, uncorrelated in time. Once one can simulate one realization of the stochastic dynamics, we may use a large sample of test particles to recover the time evolution of their smooth underlying PDF. In Fig. D1, we illustrate some examples of random walks in eccentricities. To ensure that the random walks do

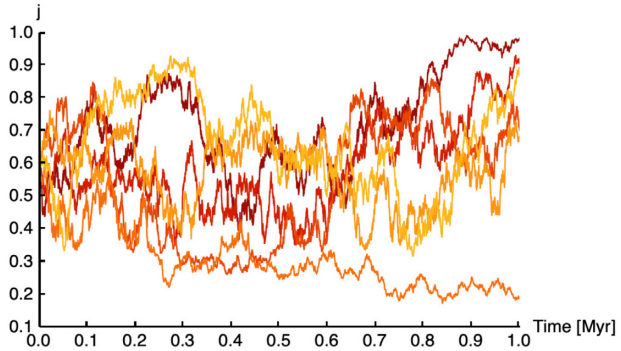

Figure D1. Illustration of stochastic random walks in eccentricities as driven by equation (D1) with a time-step $\Delta t = 0.1$ kyr. Here, the test particles all have $a = 10$ mpc, are initialized with $j = 0.6$, and evolve within the same background model as in Fig. 2.

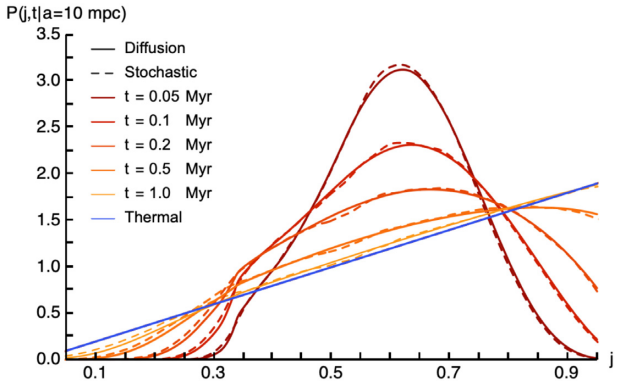

Figure D2. Comparison between the direct integration of the diffusion equation (5) (full lines) and its stochastic realization through equation (D1) (dashed lines), as a function of time, and using the same initial conditions as in Fig. D1. For the stochastic evolution, we considered a total of $N = 10^6$ test particles, evolved with the time-step $\Delta t = 0.1$ kyr. Both approaches are found to be in very good agreement, and ultimately relax, as expected, to the thermal distribution.

not wander off the range $j \in [0, 1]$, we introduced a reflective barrier at $j = 0, 1$.

Let us note that the stochastic walks from Fig. D1 do not describe any physically realistic random walks on their own, but only in an average sense. Indeed, here we have supposed that the $\xi(t)$ are uncorrelated in time, whereas they are correlated (at least on the fluctuations' coherence time) in a real physical process. However, their average over realization accurately describes the evolution of the corresponding FP equation (6).

Consequently, in Fig. D2, we use $N = 10^6$ test particles to recover the PDF at various times and compare it with that obtained from the direct integration of the diffusion equation (5) presented in the main text. The two methods yield the same result which provides us with validation. Furthermore, both methods also ultimately asymptote to the full relaxation towards the thermal PDF, $P_{\rm th}(j|a) = 2j$.

APPENDIX E: LIKELIHOOD AND LR TEST

Likelihoods measure the goodness of fit of a statistical model to a data sample. Its extremum, if it exists, is associated with models that extremize the probability of drawing the observational sample at hand. Given a a product of K joint continuous PDFs, $P_{\boldsymbol{\alpha}}(j|a_k)$, depending on a parameter $\boldsymbol{\alpha}$, and a set of i.i.d. random sampling data $\{j_{i,k}\}$, we define the likelihood of a model as

$$\mathcal{L}(\boldsymbol{\alpha}; \{j_{i,k}\}) = \prod_{k=1}^{K} \prod_{i=1}^{N} P_{\boldsymbol{\alpha}}(j_{i,k}|a_k). \tag{E1}$$

This allows us to define the likelihood ratio as

$$\lambda_{\boldsymbol{\alpha},N} = 2 \ln \left[\frac{\mathcal{L}_{\max}(\{j_{i,k}\})}{\mathcal{L}(\boldsymbol{\alpha}; \{j_{i,k}\})} \right],$$

where $\mathcal{L}_{\max}$ corresponds to the maximum likelihood within the range of explored parameters. The LR, $\lambda_{\boldsymbol{\alpha},N}$, is then a random variable, that takes its values in $[0, +\infty[$, and depends on the model's parameters, $\boldsymbol{\alpha}$.

This LR test allows us to compare models with one another, and discard those which are too unlikely. Indeed, given a model $\boldsymbol{\alpha}$, $\lambda_{\boldsymbol{\alpha},N}$ must fall close to 0 for the corresponding model to drive efficiently the eccentricity relaxation of the S-stars. Given a confidence level $0 \leq p \leq 1$, we can define from it a confidence interval $[0, \eta_p]$ within which $\lambda_{\boldsymbol{\alpha},N}$ must fall for the model to be accepted. Here, we choose η_p so that the probability $\mathbb{P}$ obeys

$$\mathbb{P}(0 \leq \lambda_{\boldsymbol{\alpha},N} \leq \eta_p) = p. \tag{E2}$$

While we do not know the exact distribution of $\lambda_{\boldsymbol{\alpha},N}$, owing to Wilks' theorem (Wilks 1938), $\lambda_{\boldsymbol{\alpha},N}$ converges to the χ^2 distribution as $K \times N \to +\infty$, and η_p obeys

$$\eta_p = 2\left[\mathrm{erf}^{-1}(p)\right]^2. \tag{E3}$$

In terms of the usual σ-levels of confidence, since the Gaussian probability of being in the interval $[-n\sigma, n\sigma]$ is $p(n\sigma) = \mathrm{erf}(n/\sqrt{2})$, then the corresponding threshold $\eta_{p(n\sigma)}$ simply becomes $\eta_{p(n\sigma)} = 2[\mathrm{erf}^{-1}\mathrm{erf}(n/\sqrt{2})]^2 = n^2$.

In practice, to validate our calculations, we also tried another non-parametric statistical estimator, namely the Kolmogorov–Smirnov distance. This led to the same conclusions. In the main text, we focused on the the maximum-likelihood estimator, because it converges asymptotically to a normal distribution and is asymptotically efficient (Wasserman 2004), leading to the $1/\sqrt{n_{\rm obs}}$ behaviour observed in Fig. 5.

This paper has been typeset from a TEX/LATEX file prepared by the author.